Role of carrier delocalization in enhancing the photostability and defect passivation of 2D/3D hybrid metal halide perovskites

Saranrat Asamo,[a, b] Whijitra Suvandee,[a, b] Ratchada Wongkanya,[a, b] Supa Hannongbua,[b, c] Nattaporn Chattham,[b, d] Chakrit Sriprachuabwong,[e] Steffen Fengler,[f] Thomas Dittrich,[g, *] and Pongthep Prajongtat[a, b, *]

[a] *Department of Materials Science, Faculty of Science, Kasetsart University, 50 Ngam Wong Wan Road, Chatuchak, Bangkok, 10900 Thailand*

[b] *Specialized Research Unit of Advanced Materials for Energy Innovation, Kasetsart University, 50 Ngam Wong Wan Road, Chatuchak, Bangkok, 10900 Thailand*

[c] *Department of Chemistry, Faculty of Science, Kasetsart University, 50 Ngam Wong Wan Road, Chatuchak, Bangkok, 10900 Thailand*

[d] *Department of Physics, Faculty of Science, Kasetsart University, 50 Ngam Wong Wan Road, Chatuchak, Bangkok, 10900 Thailand*

[e] *Energy Storage Technology Research Team (ESTT), Energy Innovation Research Group (EIRG), National Energy Technology Center (ENTEC), 114 Thailand Science Park, Phahonyothin Road, Khlong Nueng, Khlong Luang, Pathum Thani, 12120 Thailand*

[f] *Helmholtz-Zentrum Geesthacht, Zentrum für Material- und Küstenforschung, Institut für Werkstoffforschung, Max-Planck-Str.1, D-21502 Geesthacht, Germany, on leave*

[g] *Helmholtz-Zentrum Berlin für Materialien und Energie GmbH, Schwarzschildstr. 8, 12489 Berlin, Germany*

Corresponding Author

* Pongthep Prajongtat (fscipop@ku.ac.th) and Thomas Dittrich (dittrich@helmholtz-berlin.de)

Abstract

Photodegradation and defect passivation of hybrid metal halide perovskites are still challenges toward related highly stable optoelectronic devices such as solar cells. Herein, we show that photodegradation and defect density can be drastically reduced in 2D/3D perovskites by engineering the conditions for carrier delocalization. For this purpose, conjugated, partially conjugated and non-conjugated spacer molecules of similar sizes as well as n values have been systematically changed in 2D/3D perovskites based on archetypical $MAPbI_3$. The decrease of calculated HOMO-LUMO gaps of complexes with spacer molecules ($E_{\text{HL-complex}}$) correlated well with the decrease of the Urbach energy, the decrease of the trap-state density, and the strong reduction of photodegradation of 2D/3D perovskite films, whereas the photodegradation was practically independent of the n value for conjugated spacer molecules. In addition, the short circuit current density (J_{sc}) and open circuit voltage (V_{oc}) of the prepared solar cells increased with decreasing $E_{\text{HL-complex}}$; hence, maximum initial values of J_{sc} and V_{oc} larger than those of identically prepared reference solar cells based on 3D $MAPbI_3$ were reached. We also demonstrate that the photodegradation of solar cells decreased monotonously with increasing initial power conversion efficiency. Thus, delocalization by optimum coupling of electron wavefunctions between conjugated spacer molecules and binding moieties at the perovskite enhances defect passivation and strongly reduces photodegradation in 2D/3D perovskites.

Keywords: perovskite solar cell, photodegradation, carrier delocalization, spacer, conjugated molecule

1. Introduction

Hybrid metal halide perovskite solar cells (PSCs) have received tremendous attention as highly competitive alternatives to well-established silicon solar cells, mainly due to their simple and low-cost manufacturing as well as high power conversion efficiencies (PCEs), which are now comparable to those of silicon solar cells [1–5]. Nevertheless, the intrinsic instability of PSCs, driven by the rapid degradation of perovskite absorbers such as methylammonium lead iodide ($MAPbI_3$) under operating conditions, leads to a significant decline in device performance and continues to impede their practical applications [6–9]. Therefore, minimizing the degradation of perovskite absorbers is essential for the successful commercialization of PSCs. Reasons for the degradation of perovskites are chemical and photochemical reactions [10–13]. Degradation induced by chemical reactions is strongly reduced by, for example, combination of three-dimensional (3D) perovskites with layered two-dimensional (2D) perovskites (hereafter called 2D/3D perovskites) [14,15]. Moreover, a trend of decreasing degradation rate of PSCs with increasing PCE has also been reported [16]. However, the photoinduced degradation of PSCs appears to be a pervasive issue that remains challenging to address [17].

One of the most well-known layered perovskites belongs to the Dion–Jacobson 2D perovskites, which have a common formula of $S(MA)_{n-1}Pb_nI_{3n+1}$ where S and n assign a diammonium-based spacer molecule and an integer defining the thicknesses of perovskite slabs, respectively (see the structure in Fig. S1 in the Supplementary information) [18–22]. It is important to note that in practice, the pure 2D perovskites can only be created from the stoichiometric precursors with $n = 1$, otherwise 2D/3D perovskites spontaneously form [23]. Despite the fact that 2D/3D perovskites exhibit considerably improved chemical stability toward oxygen and moisture compared to 3D perovskites, they still suffer from photoinstability [24–26]. Consequently, improving the photostability of 2D/3D perovskites has become a significant research challenge that has garnered considerable attention in recent years.

Photodegradation is known from solar cells based on amorphous silicon as the Staebler–Wronski effect, which leads to the formation of metastable defects under recombination of photogenerated charge carriers at localized states [27–31]. In analogy, it can be supposed that photodegradation in perovskites originates from the recombination of photogenerated charge carriers at localized or defect states [32]. So far, point defects have been considered to be one of the dominant ionic defects in perovskite materials, involving ion vacancies such as MA^+ and I^- vacancies [33,34]. Generally, related defects generate electronic states in the bandgaps of perovskites, which act as trap states for photogenerated charge carriers [35]. Thus, enhancing the delocalization of charge carriers and reducing defect density in perovskite materials are anticipated to decrease the recombination rates of these carriers and improve the overall photostability of the materials. It has been shown that the addition of organic molecules could efficiently passivate defects in perovskite films through the interactions between the functional groups of the molecules (e.g., ammonium (NH_3^+), amino (NH_2), and carbonyl (C=O)) and defects at the perovskite grain boundaries, causing the enhanced stability of the films and related solar cells [36–39]. Furthermore, it was also highlighted that the electron distribution in passivating molecules is a key parameter that greatly affects the passivation of defects and the stability of perovskite films [40].

In 2D/3D perovskites, spacer molecules play a crucial role in the control of the charge carrier distribution and defect density [41,42]. However, most of the spacer molecules used for the fabrication of 2D/3D perovskites are insulating compounds with low dielectric constants, thus leading to restricted charge transport and nonuniform charge distribution in the perovskite films [43]. This situation could potentially facilitate charge recombination and photodegradation of the films. One viable strategy to achieve uniform charge distribution and reduce charge recombination in 2D/3D perovskites involves substituting insulating spacer molecules with conductive ones that incorporate conjugated double bonds (alternating single and double bonds) within their structures. This approach allows for the delocalization of photogenerated electrons through the conjugated spacer molecules, promoting more uniform electron distribution within the perovskite layers. A more uniform electron distribution is anticipated to enhance both the photocurrent and defect passivation in the perovskite absorber, thereby significantly improving the photocurrent and photostability of the solar cells. Conjugated spacer molecules, therefore, hold the potential to positively impact the field of 2D/3D PSCs by increasing their output current and enhancing overall solar cell performance and stability.

In this work, we combine theoretical modeling and experimental studies to unravel the role of carrier delocalization in 2D/3D perovskites for the photostability and performance of PSCs. For this purpose, different fully conjugated (4,4'-diammoniumstilbene (DAS) and 4,4'-diammoniumazobenzene (DAAB)), partially conjugated (4,4'-diammonium-1,2-diphenylethane (DADPE)) and non-conjugated (hexane-1,6-diammonium (HDA)) spacer molecules (their structures are shown in Fig. S2) were used for the fabrication of 2D/3D perovskites with the *n* values varied between 4 and 8. The conductivity and optical properties of the perovskite films as well as the performance of PSCs were characterized as a function of illumination time. We demonstrate that, in comparison with the non-conjugated and partially conjugated spacer molecules, the application of the fully conjugated spacer molecules led to a strong increase in the photoconductivity and to a reduced photodegradation of PSCs. Our observations can be attributed to the increased charge transfer between the perovskite slabs and conjugated spacer molecules and the passivation of defects.

2. Experimental methods

2.1. Synthesis of organic spacer molecules

The diammonium-based spacer molecules, including DAS, DAAB, DADPE, and HDA were synthesized via the direct conversion of amines into ammonium salts in acidic solutions. First, 2.5 mmol of 4,4'-diaminostilbene (98%, TCI chemicals), 4,4'-diaminoazobenzene (95%, Alfa Aesar), 4,4'-diamino-1,2-diphenylethane (97%, TCI chemicals) or 1,6-hexanediamine (99%, TCI chemicals) were dissolved in 30 mL of ethanol (99.9%, RCI Labscan). Subsequently, 12 mL of hydroiodic acid (HI, 57 wt% in water, Sigma-Aldrich) was gently dropped into the solutions. After the mixtures were vigorously stirred at room temperature in the dark for 24 h, 150 mL of ethyl acetate (99.5%, Merck) was slowly added into the mixtures to precipitate the resulting products. The products were filtered and washed with diethyl ether (99.5%, RCI Labscan) several times to remove the unreacted HI. To further purify the products, they were redissolved in ethanol and recrystallized using ethyl acetate. Finally, the products were dried in a vacuum oven at 60 ^{o}C for 12 h, and then stored in a N_2-filled glovebox.

2.2. Fabrication of PSCs

PSCs based on a p-i-n configuration were fabricated. The patterned indium-doped tin oxide (ITO)-coated glass substrates (20 Ω/sq, Ossila) were cleaned by sequential sonication in detergent, deionized water, acetone, and 2-propanol for 10 min each step. Afterward, a hole transport layer of poly(3,4-ethylenedioxythiophene) polystyrene sulfonate (PEDOT:PSS) was deposited onto the cleaned substrates by spin-coating 35 μL of a PEDOT:PSS solution (PH1000, Clevios) at 6000 rpm for 45 s, followed by thermal annealing at 120 °C for 15 min. The ITO/PEDOT:PSS substrates were immediately transferred into the glovebox to deposit perovskite layers. The 2 M perovskite precursor solutions were prepared by dissolving PbI_2 (99.99%, TCI chemicals), MAI (99.5%, Lumtec) and the spacer molecule (HDA, DADPE, DAS, or DAAB) with different stoichiometric ratios in a mixed solvent of *N*,*N*-dimethylformamide (99.8%, Sigma-Aldrich) and dimethyl sulfoxide (99.9%, Sigma-Aldrich) (4:1 v/v). 50 μL of the given precursor solutions were spin-coated on top of the PEDOT:PSS layer at 4000 rpm for 30 s, and then annealed at 100 °C for 30 min. As a result, ca. 600 nm-thick 2D/3D perovskite layers were formed. After letting the perovskite layers cool for 5 min, an electron transport layer of [6,6]-phenyl-C61-butyric acid methyl ester (PCBM, 99%, Lumtec) was deposited on top of the perovskite layers by spin-coating 50 μL of a 20 mg/mL PCBM solution in chlorobenzene (99.8%, Sigma-Aldrich) at 1500 rpm for 30 s. Afterward, a thin buffer layer of bathocuproine (BCP, 99%, Lumtec) was spin-coated on top of the PCBM layer from 30 μL of a 0.5 mg/mL BCP solution in isopropanol (99.5%, Sigma-Aldrich) at 4500 rpm for 30s. It should be noted that the spinning parameters and annealing conditions for layer preparation have already been optimized to achieve the best possible solar cell performance. Finally, 100 nm-thick Ag electrodes were deposited onto the BCP layer with a deposition rate of 1 Å/s by a thermal evaporator. The working area of our devices was 0.04 cm^2.

2.3. Characterization of perovskite films and solar cells

The surface morphologies of the perovskite film samples were studied by a scanning electron microscope (SEM, Quanta 450 FEI), operated at a 20 kV acceleration voltage. The functional groups of the samples were examined by an attenuated total reflectance-Fourier transform infrared (ATR-FTIR) spectrometer (Bruker Vertex 70) from 400 – 4000 cm^{-1} with a spectral resolution of 2 cm^{-1}. The X-ray diffraction patterns were obtained by a grazing incidence X-ray diffractometer (Bruker D8 Advance) with Cu Kα radiation using a step size and time of 0.02° and 0.4 s, respectively. The absorption spectra were measured by a UV-visible spectrophotometer equipped with an integrating sphere (Perkin Elmer Lambda 650) from 350 – 900 nm with a spectral resolution of 2 nm. The electrical conductivity of the samples was measured by varying the applied current from 10 nA to 10 μA in the dark and under illumination at the AM 1.5 condition using a four-point probe (Signatone S-302) equipped with a source meter (Keithley 2450) and a sun simulator (Newport, class ABB). The samples were stored in the dark or exposed to light for at least 10 min before measuring the conductivity. The average conductivity was calculated based on 5 different positions on each sample. The current density-voltage (*J-V*) curves of the PSCs were measured under 100 mW/cm^2 simulated sunlight illumination at the AM 1.5 condition using a solar cell I-V test system (Ossila). Most of the characterizations were performed in ambient air with temperature and relative humidity of 30 – 35 °C and 70 – 80%, respectively. Furthermore, photos of the layers were taken after different storage times in the dark and under illumination. The change of color has been analyzed by filtering out the red intensity and averaging it over the whole sample area.

2.4. Theoretical study

The isolated spacer molecules (S) and organic lead iodide complexes (PbI_6^{4-}–S–PbI_6^{4-}, S = HDA, DADPE, DAS, or DAAB) were theoretically investigated by spin-unrestricted density functional theory (DFT) calculations [44]. To achieve the stable geometries of the spacer molecules and complexes, full geometry optimizations were performed based on the Perdew-Burke-Ernzerhof (PBE) functional [45] and the double numerical plus polarization (DNP) basis sets [46]. For the optimization process, the convergence parameters for the energy change, maximum force, and maximum displacement were set at 2×10^{-5} Ha, 4×10^{-3} Ha Å^{-1}, and 5×10^{-3} Å, respectively. The electron distribution in the spacer molecules and complexes was calculated based on the optimized geometries by the time-dependent DFT (TDDFT) calculations with the adiabatic local-density approximation (ALDA) [47]. The binding energy (BE) among the interacting components of the PbI_6^{4-}–S–PbI_6^{4-} complexes was calculated using the below equation.

$$\mathrm{BE} = E_{\mathrm{s}} + 2E_{\mathrm{PbI}} - E_{\mathrm{complex}} \qquad (1)$$

Where E_s, E_{PbI}, and $E_{complex}$ are the total energies of the isolated spacer molecule, PbI_6^{4-}, and organic lead iodide complex, respectively. According to the equation, more positive BE values imply a stronger attraction between the spacer molecule and PbI_6^{4-} in the complex.

3. Results and discussion

Fig. 1 presents the structures and bond lengths of the HDA, DADPE, DAS, and DAAB spacer molecules, obtained by DFT calculations. All spacer molecules exhibit linear or planar geometries with slightly different molecular lengths. The DADPE, DAS, and DAAB spacer molecules have virtually the same lengths of ~12 Å, whereas the length of the HDA spacer molecule (~9 Å) is slightly shorter than those of the other three spacer molecules as a result of a smaller number of carbon atoms in the chain. This suggests that the size of the spacer molecules does not influence the charge transfer between the spacer molecules and perovskite slabs in 2D/3D perovskites because of their similar sizes. Additionally, according to their bond lengths, the DAS and DAAB spacer molecules contain fully conjugated double bonds (~1.4 Å) with the C=C (1.35 Å) and N=N (1.26 Å) linkages between two benzene rings, respectively, while the DADPE spacer molecule contains partially conjugated double bonds with the C–C (1.53 Å) linkage. In contrast, no conjugated double bonds exist in the HDA spacer molecule, for which only C–C bonds (1.52 – 1.54 Å) are present.

To verify the DFT results, the chemical bonds in the synthesized spacer molecules were studied by FTIR spectroscopy (Fig. S3). The peaks attributed to the aromatic C=C stretching (~1503 cm^{-1}) and bending (~951 cm^{-1}) modes appeared for the DADPE, DAS, and DAAB spacer molecules, but disappeared for the HDA spacer molecule. Furthermore, the peaks of the N=N (~1440 cm^{-1}) and C=N (~1640 cm^{-1}) stretching modes were observed only for the DAAB spacer molecule. Therefore, the FTIR analysis confirmed the high purity of the synthesized spacer molecules and corresponded very well to the molecules considered in the DFT analysis. Concerning the structural analyses, the spacer molecules are categorized into non-conjugated (HDA), partially conjugated (DADPE), and fully conjugated (DAS and DAAB) types.

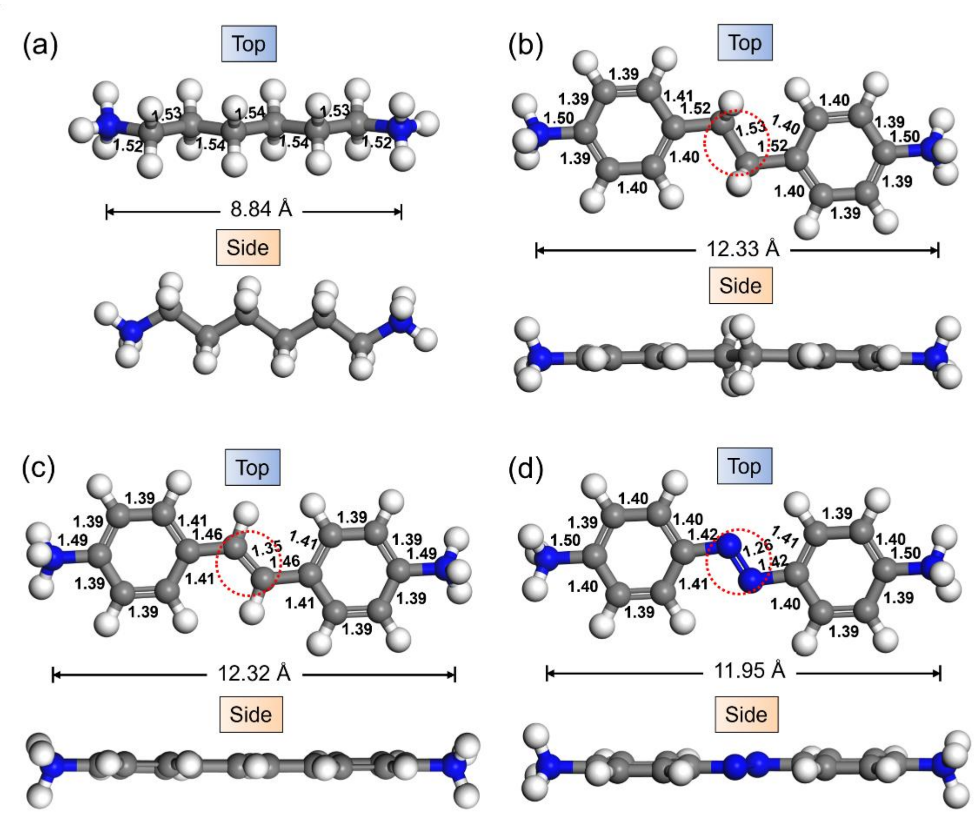

Fig. 1. Optimized structures and bond lengths (in Å) of the (a) HDA, (b) DADPE, (c) DAS, and (d) DAAB spacer molecules. C, N, and H atoms are displayed in the dark grey, blue, and white colors, respectively. The lengths of the spacer molecules are measured from the N atom of an NH_3^+ group to the N atom of the other NH_3^+ group.

To assess the electronic properties of the spacer molecules, their partial density of states (PDOS) were computed on the basis of the optimized structures shown in Fig. 1. Fig. S4 shows the PDOS of the s and p orbitals for the HDA, DADPE, DAS and DAAB spacer molecules. Due to the strong interactions of the p-orbitals in the conjugated DADPE, DAS, and DAAB spacer molecules, the lowest unoccupied molecular orbital (LUMO) levels are shifted toward the highest occupied molecular orbital (HOMO) levels compared to that of the non-conjugated HDA spacer molecule, leading to the reduction of the HOMO-LUMO gaps ($E_{HL\text{-}spacer}$). Clearly, the largest shift of the LUMO (the smallest $E_{HL\text{-}spacer}$) is found for the DAAB spacer molecule (the values of $E_{HL\text{-}spacer}$ amounted to 7.6, 4.66, 2.74, and 1.72 eV for HDA, DADPE, DAS and DAAB, respectively), suggesting that the DAAB spacer molecule exhibits the strongest p-orbitals interaction and hence, the maximum electron delocalization [48]. This is probably because the N=N linkage is relatively shorter than the C=C and C–C linkages. Incidentally, the values of $E_{HL\text{-}spacer}$ are important with respect to the formation of barriers for charge transfer from perovskite slabs into (conduction) or across (tunneling) spacer molecules.

The insets of Fig. S4 displays the simulated electron distribution in the excited states (e.g., the LUMO states) of the spacer molecules. It is clearly seen that the excited electrons can distribute over the entire structures of the DADPE, DAS, and DAAB spacer molecules due to electron delocalization. Conversely, the excited electrons localize only at the NH_3^+ groups of the HDA spacer molecule as a result of the lack of conjugated double bonds. These features specify that the conjugated double bonds are essential for enhancing the electron distribution in the spacer molecules.

We further present the distribution of electrons in the ground (e.g. HOMO) and excited (e.g. LUMO) states for organic lead iodide complexes with spacer molecules (Fig. 2). Notably, the organic lead iodide complexes can be efficiently used as the model of 2D perovskites owing to their simplicity and effectiveness [22]. To this end, the models of the complexes with a structure of PbI_6^{4-}–S–PbI_6^{4-} where S is the HDA, DADPE, DAS or DAAB spacer molecule and PbI_6^{4-} is the subunit of PbI_2 are generated and studied. We found that the electron distribution in the ground states of all complexes is localized at the PbI_6^{4-} entities (Fig. 2a, c, e, and g), whereas the excited electrons can transfer across the adjacent PbI_6^{4-} entities by injecting into the fully conjugated spacer molecules (DAS and DAAB) or even into the partially conjugated spacer molecule (DADPE). This is particularly evident in observing the orbital overlaps, i.e., the coupling between the spacer molecules and PbI_6^{4-} entities in the LUMO states of the PbI_6^{4-}–DADPE–PbI_6^{4-}, PbI_6^{4-}–DAS–PbI_6^{4-} and PbI_6^{4-}–DAAB–PbI_6^{4-} complexes (Fig. 2d, f, and h). It is important to note that the coupling causes the uniform electron distribution in the complexes and it increases with increasing the degree of electron delocalization in the spacer molecules, i.e., from PbI_6^{4-}–DADPE–PbI_6^{4-} to PbI_6^{4-}–DAS–PbI_6^{4-} and from PbI_6^{4-}–DAS–PbI_6^{4-} to PbI_6^{4-}–DAAB–PbI_6^{4-}. On the contrary, the electron distribution in the LUMO state contributes only at the PbI_6^{4-} entities in the PbI_6^{4-}–HDA–PbI_6^{4-} complex (no such coupling is observed), manifesting the inefficient charge transfer at the PbI_6^{4-}/HDA barrier and the nonuniform electron distribution in the complex (Fig. 2b). Differences in the electron distribution would lead to variations in the photovoltaic performance of PSCs.

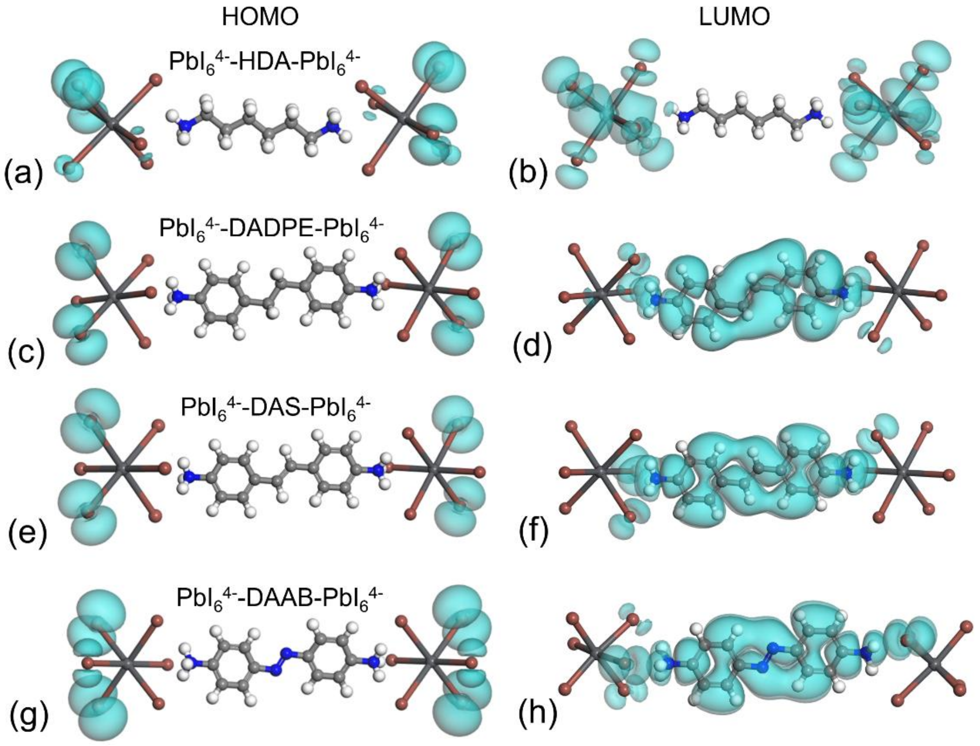

Fig. 2. Schematic illustration of the electron distributions in the HOMO and LUMO states of the (a) and (b) PbI_6^{4-}–HDA–PbI_6^{4-}, (c) and (d) PbI_6^{4-}–DADPE–PbI_6^{4-}, (e) and (f) PbI_6^{4-}–DAS–PbI_6^{4-} and (g) and (h) PbI_6^{4-}–DAAB–PbI_6^{4-} complexes.

To gain further insight into the electronic structures of the PbI_6^{4-}–S–PbI_6^{4-} complexes, the DOS of the complexes were computed, as shown in Fig. 3. For comparison, the DOS of the isolated PbI_6^{4-} were also simulated. The HOMO-LUMO gap of the isolated PbI_6^{4-} amounted to 2.81 eV, larger by ~0.4 eV compared to the bandgap of PbI_2 [49]. Moreover, the HOMO-LUMO gaps of the complexes ($E_{HL-complex}$) are smaller than that of the isolated PbI_4^{6-} (the values of $E_{HL-complex}$ amounted to 2.35, 1.52, 0.90 and 0.78 eV for the PbI_6^{4-}–HDA–PbI_6^{4-}, PbI_6^{4-}–DADPE–PbI_6^{4-}, PbI_6^{4-}–DAS–PbI_6^{4-} and PbI_6^{4-}–DAAB–PbI_6^{4-} complexes, respectively). This is because the spacer molecules create new electronic states within the HOMO-LUMO gap of the PbI_4^{6-}. The electronic states originated from the DAAB spacer molecule are closer to the HOMO state of the PbI_4^{6-} compared to those of the other spacer molecules because of the strongest coupling between the DAAB spacer molecule and PbI_6^{4-}, leading to the smallest $E_{HL-complex}$. It has been expected that the smaller $E_{HL-complex}$ value would lead to the greater charge transfer between perovskite slabs and spacer molecules in 2D/3D perovskites.

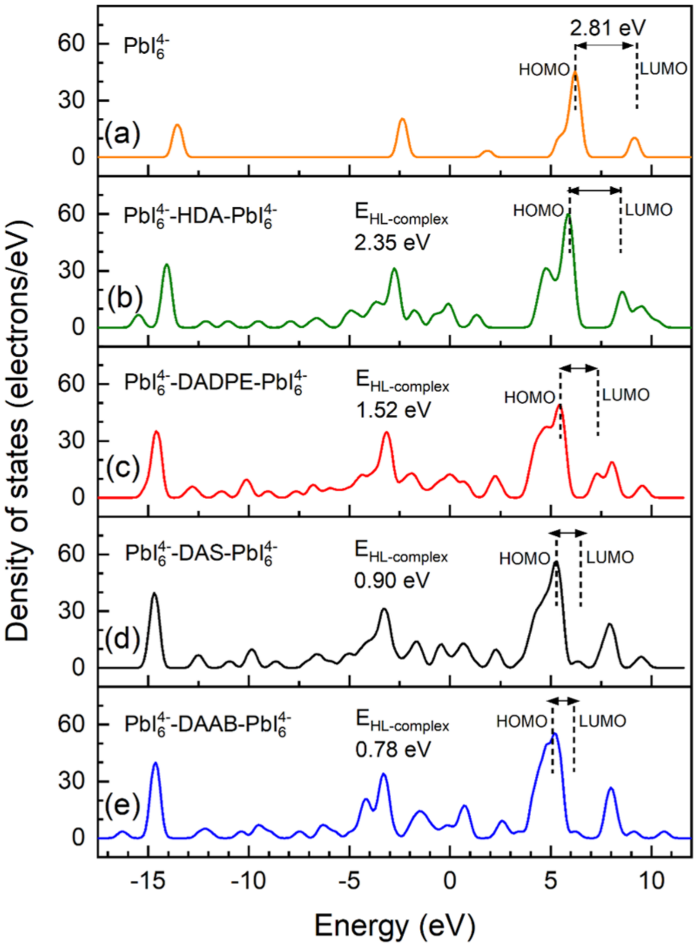

Fig. 3. Density of states of the (a) PbI_6^{4-}, (b) PbI_6^{4-}–HDA–PbI_6^{4-}, (c) PbI_6^{4-}–DADPE–PbI_6^{4-}, (d) PbI_6^{4-}–DAS–PbI_6^{4-} and (e) PbI_6^{4-}–DAAB–PbI_6^{4-} complexes.

To consolidate our discussion, we prepared the 2D/3D $(S)(MA)_{n-1}Pb_nI_{3n+1}$ perovskite films (S is HDA, DADPE, DAS or DAAB, and $n = 4 – 8$) using a one-step spin-coating method (see the details in the Experimental method). The perovskite films were deposited onto the indium-doped tin oxide (ITO)-coated glasses, having a uniform thickness of ~600 nm (Fig. S5). Although the spacer molecules used in the films are different, the surface morphologies and grain size of the films are similar (see, for example, the scanning electron microscope (SEM) images of the $n = 4$ films in Fig. S6), suggesting that the spacer molecules do not significantly influence the growth of the perovskite films and that the morphologies will not affect the film conductivity. The incorporation of the spacer molecules into the films is confirmed by the appearance of their characteristic peaks, for instance, aromatic C=C stretching (~1506 cm^{-1}) and bending (~996 cm^{-1}) in the FTIR spectra of the films (Fig. S7). In addition, the X-ray diffraction (XRD) patterns (Fig. S8) reveal that the films are composed of 2D and 3D perovskites, assigned as the minor and major phases, respectively. Nevertheless, the amounts of the 2D perovskites in the films decrease when the *n* values increase, caused by the enlargement of the perovskite dimension. Moreover, there is no shift of the XRD peaks of the 3D $MAPbI_3$ perovskite (at 14.3°, 28.2°, and 31.8°) even when the spacer molecules and *n* values of the films are changed, implying that the spacer molecules are preferably located at the boundaries of the 3D perovskite grains.

Since the thicknesses of all films are very similar, the conductivities of all samples can be directly compared. The conductivity of the 3D $MAPbI_3$ control sample was observed to be 1.53×10^{-7} S/cm in the dark and 5.36×10^{-6} S/cm under illumination. Fig. 4 shows the dependencies of the conductivities in the dark and under illumination on the *n* value for the 2D/3D perovskite films based on the different spacer molecules. For the films based on HDA spacer molecules, both the conductivities in the dark and under illumination increased with increasing *n* values from 2.48×10^{-8} (in the dark) and 2.88×10^{-8} (under illumination) S/cm at $n = 4$ to 4.34×10^{-8} (in the dark) and 4.42×10^{-8} (under illumination) S/cm at $n = 8$. These values were significantly smaller than those of the 3D $MAPbI_3$ control sample. The increase of the conductivity with increasing *n* values means that the conductivity increases with decreasing amount of HDA spacer molecules in the sample. Therefore, HDA spacer molecules led to a reduction of the conductivity in the 2D/3D perovskite film, confirming the poor charge transfer between the perovskite slabs and HDA spacer molecules.

For the 2D/3D perovskite films based on DAAB spacer molecules, the conductivities in the dark and under illumination decreased with increasing *n* values from 6.63×10^{-8} (in the dark) and 2.08×10^{-6} (under illumination) S/cm at $n = 4$ to 3.83×10^{-8} (in the dark) and 9.58×10^{-8} (under illumination) S/cm at $n = 8$. The conductivities in the dark are of the same order as for the 2D/3D perovskite films based on HDA spacer molecules, whereas the conductivity under illumination was much higher for the 2D/3D perovskite film based on DAAB spacer molecules. Especially, the strong increase of the conductivity under illumination with decreasing *n* values indicates that the conductivity increases with increasing the amount of DAAB spacer molecules in the sample, i.e. the presence of DAAB spacer molecules enhanced the conductivity due to the efficient electron delocalization.

For the 2D/3D perovskite films based on DADPE spacer molecules, the conductivity in the dark increased with increasing *n* values from $6.29\mathrm{x}10^{-8}$ at $n = 4$ to $1.99\mathrm{x}10^{-7}$ S/cm at $n = 8$ which was even higher than the dark conductivity of the 3D $\mathrm{MAPbI_3}$ control sample. This means that DADPE spacer molecules limited much less the conductivity than HDA spacer molecules. The conductivity under illumination first decreased with increasing *n* values up to $n = 6$ and afterward increased with increasing *n* values which gives evidence for some intermediate influence of DADPE spacer molecules.

For the 2D/3D perovskite films based on DAS spacer molecules, the conductivity in the dark increased from $6.50\mathrm{x}10^{-8}$ up to $1.49\mathrm{x}10^{-7}$ S/cm with increasing *n* values from 4 to 8, which was similar to the films based on DADPE spacer molecules. On the contrary, the conductivity under illumination decreased with increasing *n* values from $8.55\mathrm{x}10^{-7}$ S/cm at $n = 4$ to $1.92\mathrm{x}10^{-7}$ S/cm at $n = 7$ or $2.90\mathrm{x}10^{-7}$ S/cm at $n = 8$, i.e. an increasing amount of spacer molecules led to a decrease of the conductivity in the dark, but to an increase of the conductivity under illumination similar to the case of DAAB spacer molecules. Based on the above results, we conclude that the perovskite films based on fully conjugated spacer molecules (DAAB and DAS) exhibit the efficient electron delocalization and much more uniform electron distribution compared to the films based on partially conjugated (DADPE) and non-conjugated (HDA) spacer molecules.

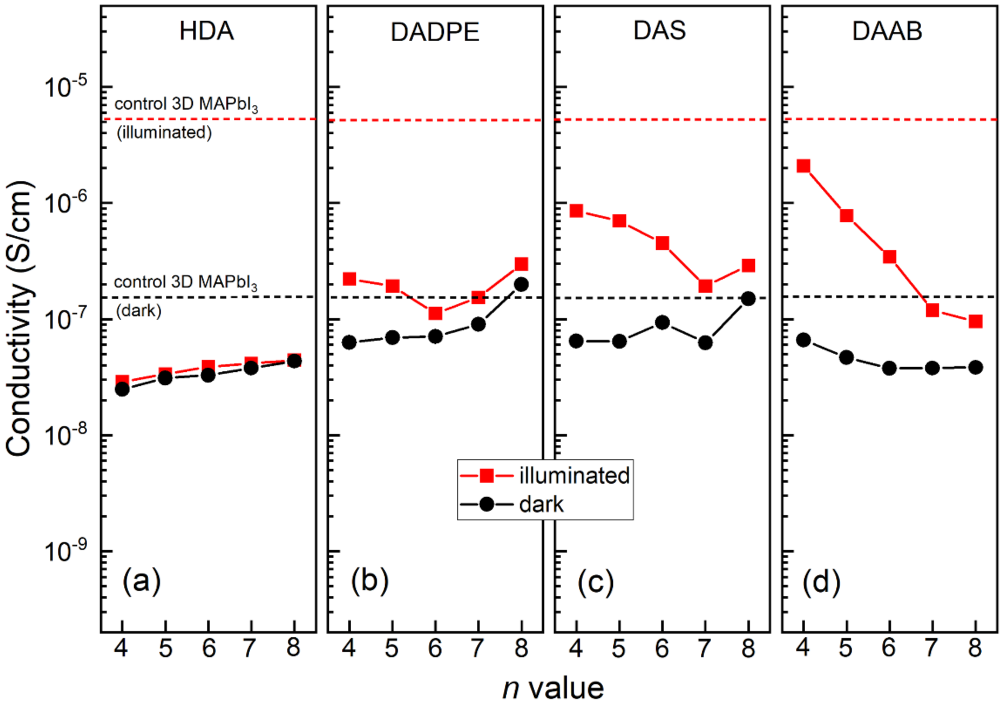

Fig. 4. Dependencies of the conductivity measured with a 4-point-probe in the dark (black circles) and under illumination (red squares) on the *n* value for the 2D/3D perovskite films based on HDA, DADPE, DAS and DAAB spacer molecules ((a) – (d), respectively). The dashed black and red lines mark the conductivity in the dark and under illumination, respectively, for the 3D $MAPbI_3$ control sample.

2D/3D perovskite films based on HDA, DADPE, DAS and DAAB spacer molecules were stored under illumination with a sun simulator in ambient air. Photos were taken from each sample as a function of time (see the upper part of Fig. 5). It turned out that 2D/3D perovskite films based on HDA spacer molecules changed their color from dark brownish to yellowish within the first day under illumination, i.e. the sample showed strong light-induced structural degradation. The 2D/3D perovskite films based on DADPE spacer molecules started to change their color within the second day of storage under illumination, whereas slight changes appeared in the color of the 2D/3D perovskite films based on DAS spacer molecules within the third day. In contrast, the 2D/3D perovskite films based on DAAB spacer molecules did not change their color within 3 days under illumination. To prove that the degradation of the films shown in Fig. 5 is mainly caused by illumination, a new set of films was prepared and stored in the dark under the same environmental conditions. It was found that the color of all films was still dark brownish even when they were stored in the dark for more than 72 h (Fig. S9), confirming that the degradation of the films was primarily attributed to illumination rather than humidity.

The lower part of Fig. 5 presents the dependencies of the red intensity deduced by the color analysis on the illumination time for the 2D/3D perovskite films based on HDA, DADPE, DAS and DAAB spacer molecules ((a) – (d), respectively). For the *n* value of 4 of the 2D/3D perovskite films based on HDA spacer molecules, a drastic increase of the red intensity started within the first two hours which was by far the fastest degradation of all 2D/3D perovskite films. For the *n* value of 5 – 8 of the 2D/3D perovskite films based on HDA spacer molecules, the dependencies of the red intensity on illumination time were very similar whereas the red intensities increased drastically at times between 5 and 9 h.

For the 2D/3D perovskite films based on DADPE, DAS and DAAB spacer molecules, the dependencies of the red intensity on the illumination time were independent of the *n* value. Furthermore, the red-intensities of these samples changed much less than for the 2D/3D perovskite films based on HDA spacer molecules after long illumination times, i.e. degradation was drastically reduced for the 2D/3D perovskite films based on DADPE, DAS and DAAB spacer molecules. This finding emphasizes the role of carrier delocalization in retarding the photodegradation of the films. Fig. S10 shows the XRD patterns of these films, revealing the transformation of $MAPbI_3$ (2θ ~14.3°) into PbI_2 (2θ ~12.5°) over varying illumination durations. The film based on HDA spacer molecules demonstrated a rapid transformation within 24 hours of illumination. In contrast, the films based on DADPE and DAS spacer molecules displayed a gradual transformation, whereas no transformation was observed in the film based on DAAB spacer molecules. These results are consistent with the red-intensity analysis that the light-induced structural degradation for the films based on HDA spacer molecules was much faster than that for the films based on DADPE, DAS, and DAAB.

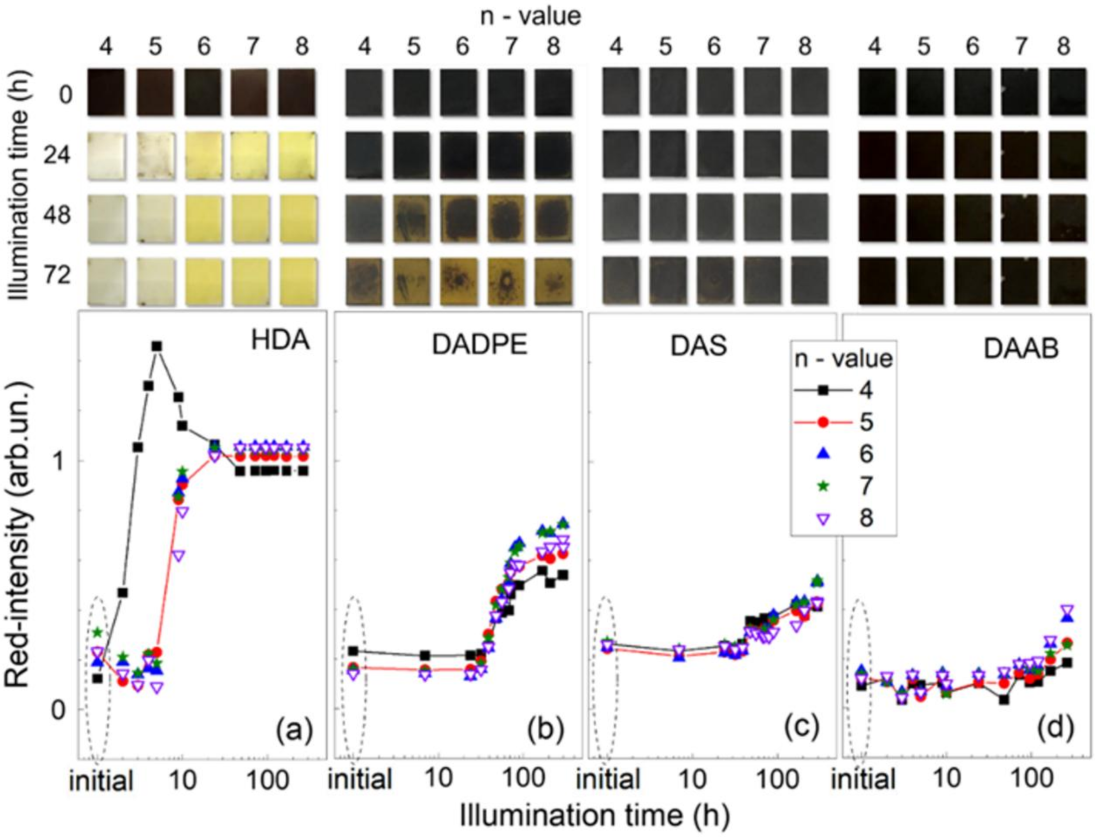

Fig. 5. Photographs of the 2D/3D perovskite films with *n* = 4 – 8 taken after different illumination times (upper part) and dependencies of the red-intensity on the illumination time (lower part) for the 2D/3D

perovskite films with $n = 4 – 8$ (black squares, red circles, blue triangles, green stars and open violet triangles) based on HDA, DADPE, DAS and DAAB spacer molecules ((a) – (d), respectively).

To investigate the influence of carrier delocalization on the performance and stability of PSCs, all devices were prepared under identical conditions for the 2D/3D perovskites with the n value of 4 and for the 3D $MAPbI_3$ control sample. A cross-sectional SEM image of the prepared devices is shown in Fig. S11a, revealing that the thicknesses of the PEDOT:PSS, perovskite, PCBM, and Ag layers were ~100 nm, 600 nm, 50 nm, and 100 nm, respectively. Notably, due to the extremely thin nature of the BCP layer, its thickness was estimated to be less than 10 nm. Fig. S11b illustrates the current density-voltage (J-V) curves and extracted photovoltaic parameters of the champion devices for each spacer molecule and for the 3D $MAPbI_3$ control sample, measured under AM 1.5 G illumination at relative humidity (RH) of ~70%. We notice that the relatively high PCEs observed for the devices based on fully conjugated (DAAB and DAS) and partially conjugated (DADPE) spacer molecules are attributed to the enhanced short circuit current density (J_{sc}), which is in line with the conductivity results. It was also found that the device characteristics correlated very well with the $E_{HL\text{-}complex}$ values. Fig. 6a shows the correlations between $E_{HL\text{-}complex}$ and J_{sc} and the open circuit voltage (V_{oc}) averaged from five devices. The values of J_{sc} decreased continuously from ~24.4 mA/cm² for the lowest $E_{HL\text{-}complex}$ (for the complex with DAAB) to ~11.5 mA/cm² for the highest $E_{HL\text{-}complex}$ (for the complex with HDA). For comparison, J_{sc} was ~23.2 mA/cm² for the 3D $MAPbI_3$ control device. Hence, it is possible to achieve similar or even higher values of J_{sc} for the 2D/3D perovskite film based on DAAB spacer molecules than for the 3D $MAPbI_3$ control device. Moreover, the value of V_{oc} amounted to ~0.87 V for the 3D $MAPbI_3$ control device. For comparison, V_{oc} was ~0.92, 0.86, 0.81, and 0.79 V for the devices based on DAAB, DAS, DADPE, and HDA spacer molecules, respectively. These strongly suggest that J_{sc} and V_{oc} can be well enhanced by passivating recombination active trap states with conjugated spacer molecules and that the design of the spacer molecules is decisive.

To probe the trap density (N_t) in the 2D/3D perovskite films, the space-charge-limited current (SCLC) measurements of hole-only devices, ITO/PEDOT:PSS/perovskite/P3HT/Ag, were performed

[50]. The value of N_t can be calculated from the trap-filled limit voltage (V_{TFL}) achieved by the transition point between the ohmic and trap-filled limit regions in a dark *J-V* curve using the following equation.

$$V_{\mathrm{TFL}} = \frac{eN_t d^2}{2\varepsilon\varepsilon_0} \qquad (2)$$

Where e is the elementary charge, d is the thickness of the perovskite layer, ε is the dielectric constant of the perovskite, and ε_0 is the vacuum permittivity.

As can be seen from Fig. S12a, the V_{TFL} obtained from the devices based on HDA, DADPE, DAS, DAAB spacer molecules, and from the control device are found to be 0.43, 0.40, 0.36, 0.30, and 0.38 V, respectively. Accordingly, the N_t values are 9.94×10^{14}, 9.25×10^{14}, 8.33×10^{14}, 6.94×10^{14}, and 8.79×10^{14} cm^{-3}, respectively (Fig. 6b). The devices based on HDA and DADPE spacer molecules exhibited higher N_t values compared to the devices based on DAS and DAAB spacer molecules. These results are in good agreement with the trends of J_{sc} and V_{oc} of the solar cells that were previously discussed.

We also examined the trap states near the bandgaps of the 2D/3D perovskite films fabricated from different spacer molecules by estimating the Urbach energy (E_u) from their UV-vis absorption spectra (Fig. S12b) using the following equation.

$$\alpha = \alpha_0 \exp\left(\frac{E}{E_{\mathrm{u}}}\right) \qquad (3)$$

Where α is the absorption coefficient of the perovskite, E is the photon energy. When plotting between ln(α) and E, the E_u value can be achieved from the reciprocal of the fitting slope. Moreover, the E_u value is directly proportional to the trap density near the bandgap of the perovskite [32].

The E_u values of the 2D/3D perovskite films based on HDA, DADPE, DAS and DAAB spacer molecules, and of the 3D $MAPbI_3$ control film are 55.6, 38.7, 33.4, 31.8, and 39.6 meV, respectively (Fig. 6b). This reveals that the films based on conjugated spacer molecules have higher electronic quality compared to the control films and the films based on nonconjugated spacer molecules due to the lower trap density, which is consistent with the N_t values obtained from the SCLC measurements. Therefore, we deduce that the uniform electron distribution in the 2D/3D perovskite films based on conjugated spacer molecules could efficiently passivate the positively charged defects, such as the I^- vacancies at the perovskite grain boundaries via the strong electrostatic interactions. To confirm this, the interactions between the spacer molecules and an iodide vacancy in the PbI_5^{3-} cluster (the model represents the iodide vacancy) are illustrated in Fig. S13. We found that the DAAB and HDA spacer molecules demonstrate the strongest and lowest binding strength to the PbI_5^{3-} with the BE of 11.04 and 9.50 eV, respectively, providing clear evidence of the effective passivation of the charged defects through the uniform electron distribution in the spacer molecules.

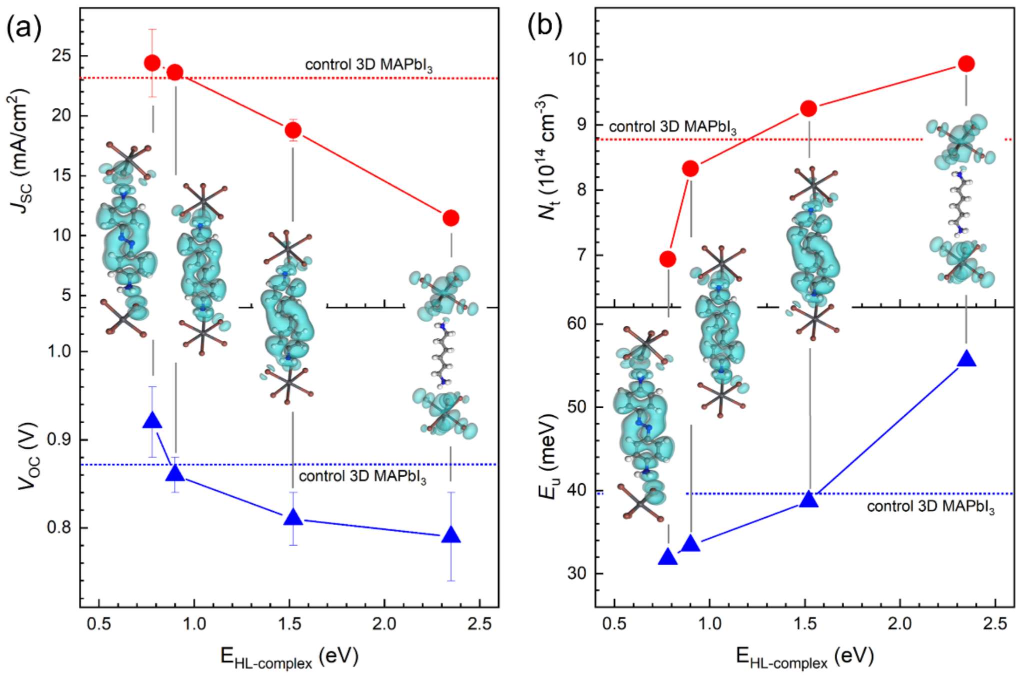

Fig. 6. Correlations of (a) the short circuit current densities (J_{sc}) and the open circuit voltages (V_{oc}) of 2D/3D PSCs averaged from five devices and (b) of the trap density (N_t) of hole-only devices and the Urbach energy (E_u) of perovskite films with the values of $E_{HL\text{-}complex}$ obtained from DFT analysis of the PbI_6^{4-}–HDA–PbI_6^{4-}, PbI_6^{4-}–DADPE–PbI_6^{4-}, PbI_6^{4-}–DAS–PbI_6^{4-} and PbI_6^{4-}–DAAB–PbI_6^{4-} complexes (insets: schematic illustration of the electron distributions in the LUMO states of the corresponding complexes). The red and blue dotted lines mark the values for the 3D $MAPbI_3$ control samples.

The stability tests of the unencapsulated devices stored in the dark and under illumination were performed for more than 1000 h (Fig. 7a and b, respectively). Clearly, the PCEs of the devices stored in the dark were quite stable, in which the PCEs remained ~90% of their initial values for all devices. However, when the devices were illuminated continuously for 1000 h, their PCEs were obviously reduced, especially for the device based on HDA spacer molecules (the PCE was dramatically reduced to 35% of its initial value). At the same time, the devices based on DADPE, DAS, and DAAB spacer molecules exhibited much smaller PCE reduction (the devices retained 43, 50, and 68% of their initial PCE values, respectively). These results are consistent with the enhanced stability of the films based on conjugated spacer molecules (Fig. 5), strongly confirming that the electron delocalization in the 2D/3D perovskite films could greatly enhance the device photostability by reducing the photodegradation of the perovskite films.

The relative change of the PCE after illumination for 1000 h (rel. PCE_{1000h}) has been correlated with the initial PCE values of the devices (Fig. 7c). The initial values of the PCE amounted to ~4.5, 7.9, 11.4, and 12.6% for the solar cells with 2D/3D perovskite films (n = 4) based on HDA, DADPE, DAS, and DAAB spacer molecules, respectively. This means that the initial PCE increased monotonously with increasing electron delocalization in the films. Furthermore, the rel. PCE_{1000h} increased monotonously with increasing initial PCE. Fig. 7 (c) also plots some high values of rel. PCE_{1000h} and initial PCE published by different groups in recent years for different kinds of metal halide perovskites. It can be seen that the values obtained within this work are within the corridor for reaching high stability at a high initial PCE.

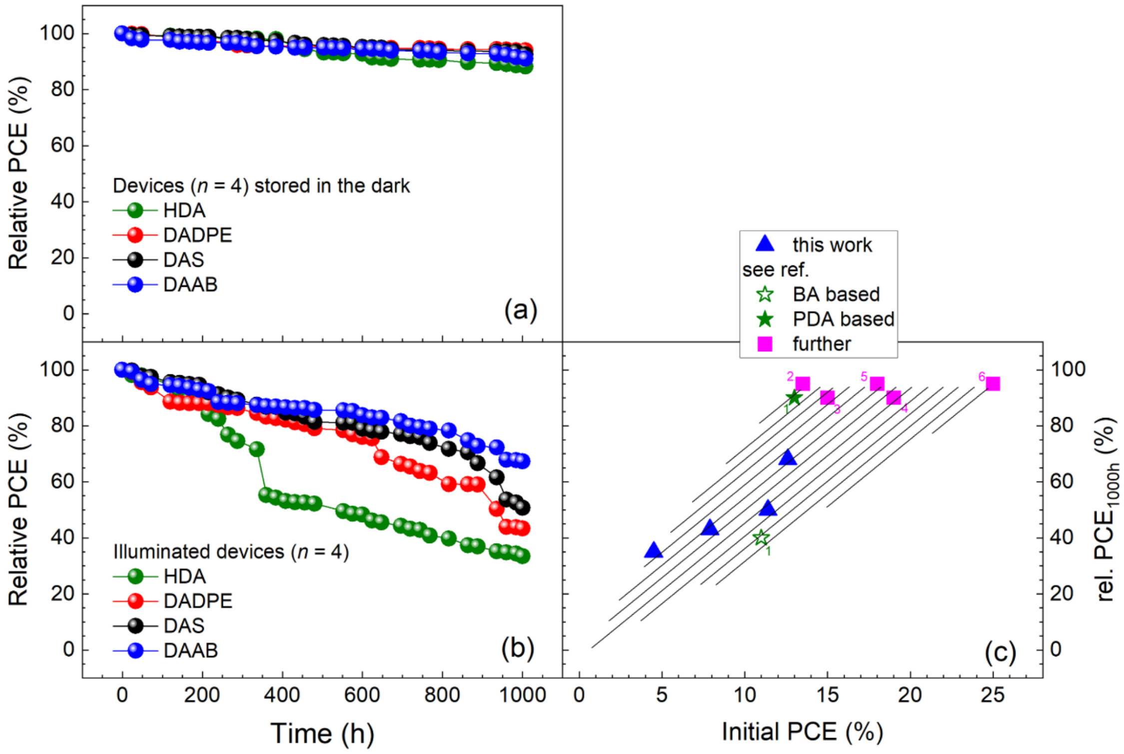

Fig. 7. Stability tests of (a) the devices stored in the dark and of (b) the devices exposed to light for more than 1000 h. (c) correlation of the rel. $\text{PCE}_{1000\text{h}}$ with the initial PCE of this work and of some results on different kinds of metal halide perovskite-based solar cells published by other groups (1: Ma (2018)[41], 2: Ahmad (2019)[51], 3: Zhao (2020)[52], 4: Xu (2021)[53], 5: Li (2022)[54], 6: Liu (2023)[55]). Lines are guides for the eyes, the hatched area describes a corridor for reaching the highest stability with increasing initial PCE.

4. Conclusions

In summary, fully conjugated (e.g., DAAB and DAS), partially conjugated (e.g., DADPE), and non-conjugated (e.g., HDA) spacer molecules of comparable sizes were employed in the fabrication of 2D/3D perovskite layers and PSCs. Analyses conducted using DFT and conductivity measurements revealed that charge transfer between the perovskite slabs and spacer molecules in 2D/3D perovskites significantly improved with increased electronic coupling. Compared to non-conjugated and partially conjugated spacer molecules, fully conjugated spacer molecules not only enhanced the photostability but also increased the photocurrent of PSCs. This enhancement is primarily attributed to the great charge transfer and efficient electron delocalization within the perovskite layers. Additionally, the uniform electron distribution achieved with fully conjugated spacer molecules facilitated effective passivation of trap states in the perovskite layers, as evidenced by the marked reduction in E_u and N_t values. Consequently, PSCs incorporating fully conjugated spacer molecules exhibited improved photovoltage. Furthermore, we demonstrated that the photodegradation of PSCs decreased as their initial PCE values increased. Our findings suggest that carrier delocalization is crucial for the development of photostable and efficient PSCs.

AUTHOR INFORMATION

Corresponding author

*P. Prajongtat. E-mail: fscipop@ku.ac.th

*Th. Dittrich. E-mail: dittrich@helmholtz-berlin.de

Notes

The authors declare no competing financial interest.

Acknowledgements

This work was supported by the Kasetsart University Research and Development Institute (FF(KU)51.67 and FF(KU)27.67), the National Science, Research and Innovation Fund (NSRF) via the Program Management Unit for Human Resources & Institutional Development, Research and Innovation (B11F660024), and National Nanotechnology Center (NANOTEC, Thailand). SA and RW are grateful to the Thailand Graduate Institute of Science and Technology (TGIST) and the Capacity Building of KU Students on Internationalization program: KUCSI.

References

(1) C. Case, N. Beaumont, D. Kirk, Industrial insights into perovskite photovoltaics, ACS Energy Lett. 4 (2019) 2760–2762.

(2) E. Velilla, D. Ramirez, J.-I. Uribe, J. F. Montoya, F. Jaramillo, Outdoor performance of perovskite solar technology: silicon comparison and competitive advantages at different irradiances, Sol. Energy. Mater. Sol. Cells 191 (2019) 15–20.

(3) P. Holzhey, M. Pretti, S. Collavini, N. L. Chang, M. Saliba, Toward commercialization with lightweight, flexible perovskite solar cells for residential photovoltaics, Joule 7 (2023) 257–271.

(4) Z. Song, C. L. McElvany, A. B. Phillips, I. Celik, P. W. Krantz, S. C. Watthage, G. K. Liyanage, D. Apul, M. J. Heben, A technoeconomic analysis of perovskite solar module manufacturing with low-cost materials and techniques, Energy Environ. Sci. 10 (2017) 1297–1305.

(5) L. McGovern, E. Alarcón-Lladó, E. C. Garnett, B. Ehrler, B. van der Zwaan, Perovskite solar modules for the residential sector, ACS Energy Lett. 8 (2023) 4862–4866.

(6) P. Toloueinia, H. Khassaf, A. S. Amin, Z. M. Tobin, S. P. Alpay, S. L. Suib, Moisture-induced structural degradation in methylammonium lead iodide perovskite thin films, ACS Appl. Energy Mater. 3 (2020) 8240–8248.

(7) G. Abdelmageed, C. Mackeen, K. Hellier, L. Jewell, L. Seymour, M. Tingwald, F. Bridges, J. Z. Zhang, S. Carter, Effect of temperature on light induced degradation in methylammonium lead iodide perovskite thin films and solar cells, Sol. Energy Mater. Sol. Cells 174 (2018) 566–571.

(8) R. Guo, M. V. Khenkin, G. E. Arnaoutakis, N. A. Samoylova, J. Barbé, H. K. H. Lee, W. C. Tsoi, E. A. Katz, Initial stages of photodegradation of $MAPbI_3$ perovskite: accelerated aging with concentrated sunlight, Sol. RRL 4 (2020) 1900270.

(9) Y.-B. Lu, W.-Y. Cong, C. Guan, H. Sun, Y. Xin, K. Wang, S. Song, Light enhanced moisture degradation of perovskite solar cell material $CH_3NH_3PbI_3$, J. Mater. Chem. A 7 (2019) 27469–27474.

(10) C. C. Boyd, R. Cheacharoen, T. Leijtens, M. D. McGehee, Understanding degradation mechanisms and improving stability of perovskite photovoltaics, Chem. Rev. 119 (2019) 3418–3451.

(11) D. Zhang, D. Li, Y. Hu, A. Mei, H. Han, Degradation pathways in perovskite solar cells and how to meet international standards, Commun. Mater. 58 (2022) 1–14.

(12) J. Bisquert, E. J. Juarez-Perez, The cause of degradation of perovskite solar cells, J. Phys. Chem. Lett. 10 (2019) 5889–5891.

(13) Q. Emery, M. Remec, G. Paramasivam, S. Janke, J. Dagar, C. Ulbrich, R. Schlatmann, B. Stannowski, E. Unger, M. Khenkin, Encapsulation and outdoor testing of perovskite solar cells: comparing industrially relevant process with a simplified lab procedure, ACS Appl. Mater. Interfaces 14 (2022) 5159–5167.

(14) I. Metcalf, S. Sidhik, H. Zhang, A. Agrawal, J. Persaud, J. Hou, J. Even, A. D. Mohite, Synergy of 3D and 2D perovskites for durable, efficient solar cells and beyond, Chem. Rev. 123 (2023) 9565–9652.

(15) G. Grancini, C. Roldán-Carmona, I. Zimmermann, E. Mosconi, X. Lee, D. Martineau, S. Narbey, F. Oswald, F. De Angelis, M. Graetzel, M. K. Nazeeruddin, One-year stable perovskite solar cells by 2D/3D interface engineering, Nat. Commun. 8 (2017) 15684.

(16) N. T. P. Hartono, H. Köbler, P. Graniero, M. Khenkin, R. Schlatmann, C. Ulbrich, A. Abate, Stability follows efficiency based on the analysis of a large perovskite solar cells ageing dataset, Nat. Commun. 14 (2023) 4869.

(17) Z. Wang, Z. Zhang, L. Xie, S. Wang, C. Yang, C. Fang, F. Hao, Recent advances and perspectives of photostability for halide perovskite solar cells, Adv. Opt. Mater. 10 (2022) 2101822.

(18) L. Mao, W. Ke, L. Pedesseau, Y. Wu, C. Katan, J. Even, M. R. Wasielewski, C. C. Stoumpos, M. G. Kanatzidis, Hybrid Dion-Jacobson 2D lead iodide perovskites, J. Am. Chem. Soc. 140 (2018) 3775–3783.

(19) D. Wang, S.-C. Chen, Q. Zheng, Enhancing the efficiency and stability of two-dimensional Dion-Jacobson perovskite solar cells using a fluorinated diammonium spacer, J. Mater. Chem. A. 9 (2021) 11778–11786.

(20) H. Fu, Dion-Jacobson halide perovskites for photovoltaic and photodetection applications, J. Mater. Chem. C 9 (2021) 6378–6394.

(21) X. Jiang, J. Zhang, S. Ahmad, D. Tu, X. Liu, G. Jia, X. Guo, C. Li, Dion-Jacobson 2D-3D perovskite solar cells with improved efficiency and stability, Nano Energy 75 (2020) 104892.

(22) R. Wongkanya, S. Asamo, D. Dechtrirat, J. Sudchanham, N. Srisamran, C. Sriprachuabwong, A. Tuantranont, N. Chattham, S. Hannongbua, P. Prajongtat, Enhancing the stability and performance of two-dimensional perovskite solar cells *via* double-step homogeneous precursor mixing, ACS Appl. Energy Mater. 5 (2022) 12415–12426.

(23) R. Vázquez-Cárdenas, J. Rodríguez-Romero, C. Echeverría-Arrondo, J. Sanchez-Diaz, V. S. Chirvony, J. P. Martínez-Pastor, P. Díaz-Leyva, J. Reyes-Gómez, I. Zarazua, I. Mora-Seró, Suppressing the formation of high *n*-phase and 3D perovskites in the fabrication of Ruddlesden-Popper perovskite thin films by bulky organic cation engineering, Chem. Mater. 34 (2022) 3076–3088.

(24) F. Fiorentino, M. D. Albaqami, I. Poli, A. Petrozza, Thermal- and light-induced evolution of the 2D/3D interface in lead-halide perovskite films, ACS Appl. Mater. Interfaces 14 (2022) 34180–34188.

(25) K. Datta, A. Caiazzo, M. A. Hope, J. Li, A. Mishra, M. Cordova, Z. Chen, L. Emsley, M. M. Wienk, R. A. J. Janssen, Light-induced halide segregation in 2D and quasi-2D mixed-halide perovskites, ACS Energy Lett. 8 (2023) 1662–1670.

(26) H.-H. Fang, J. Yang, S. Tao, S. Adjokatse, M. E. Kamminga, J. Ye, G. R. Blake, J. Even, M. A. Loi, Unravelling light-induced degradation of layered perovskite crystals and design of efficient encapsulation for improved photostability, Adv. Funct. Mater. 28 (**2018**) 1800305.

(27) Staebler, D. L., Wronski, C. R., Reversible conductivity changes in discharge-produced amorphous Si, Appl. Phys. Lett. (1977) 31, 292–294.

(28) Wang, Y., Han, X., Zhu, F., Hou, G., Ren, H., Zhang, K., Xue, J., Sun, J., Zhao, Y., Geng, X., Light induced degradation of microcrystalline silicon solar cells, J. Non-Cryst. Solids (2006) 352, 1909–1912.

(29) Santos, P. V., Jackson, W. B., Dispersive model for the kinetics of light-induced defects in a-Si:H, Phys. Rev. B (1991) 44, 10937.

(30) Stutzmann, M., Jackson, W. B., Tsai, C. C., Kinetics of the Staebler-Wronski effect in hydrogenated amorphous silicon, Appl. Phys. Lett. (1984) 45, 1075–1077.

(31) Stutzmann, M., Jackson, W. B., Tsai, C, C., Light-induced metastable defects in hydrogenated amorphous silicon: A systematic study, Phys. Rev. B (1985) 32, 23–47.

(32) Prajongtat, P., Dittrich, Th., Precipitation of $CH_3NH_3PbCl_3$ in $CH_3NH_3PbI_3$ and its impact on modulated charge separation, J. Phys. Chem. C (2015) 119, 9926–9933.

(33) Motti, S. G., Meggiolaro, D., Martani, S., Sorrentino, R., Barker, A. J., De Angelis, F., Petrozza, A., Defect activity in metal-halide perovskites, Adv. Mater. (2019) 31, 1901183.

(34) Aydin, E., De Bastiani, M., De Wolf, S., Defect and contact passivation for perovskite solar cells, Adv. Mater. (2019) 31, 1900428.

(35) Guo, Y., Ma, J., Lei, H., Yao, F., Li, B., Xiong, L., Fang, G., Enhanced performance of perovskite solar cells *via* anti-solvent nonfullerene lewis base IT-4F induced trap-passivation, J. Mater. Chem. A (2018) 8, 5919–5925.

(36) Wang, M., Sun, H., Wang, M., Meng, L., Li, L., Uracil induced simultaneously strengthening grain boundaries and interfaces enables high-performance perovskite solar cells with superior operational stability, Adv. Mater. (2024) 36, 2306415.

(37) Hsiao, K.-C., Jao, M.-H., Li, B.-T., Lin, T.-H., Liao, S. H.-C., Wu, M.-C., Su, W.-F., Enhancing efficiency and stability of hot casting p-i-n perovskite solar cell via dipolar ion passivation, ACS Appl. Energy Mater. (2019) 2, 4821–4832.

(38) Liu, T., Guo, J., Lu, D., Xu, Z., Fu, Q., Zheng, N., Xie, Z., Wan, X., Zhang, X., Liu, Y., Chen, Y., Spacer engineering using aromatic formamidinium in 2D/3D hybrid perovskites for highly efficient solar cells, ACS Nano (2021) 15, 7811–7820.

(39) Lin, C.-T., De Rossi, F., Kim, J., Baker, J., Ngiam, J., Xu, B., Pont, S., Aristidou, N., Haque, S. A., Watson, T., McLachlan, M. A., Durrant, J. R., Evidence for surface defect passivation as the origin of the remarkable photostability of unencapsulated perovskite solar cells employing aminovaleric acid as a processing additive, J. Mater. Chem. A (2019) 7, 3006–3011.

(40) Xin, D., Tie, S., Yuan, R., Zheng, X., Zhu, J., Zhang, W.-H., Defect passivation in hybrid perovskite solar cells by tailoring the electron density distribution in passivation molecules, ACS Appl. Mater. Interfaces (2019) 11, 44233–44240.

(41) Ma, C., Shen, D., Ng, T.-W., Lo, M.-F., Lee, C.-S., 2D perovskites with short interlayer distance for high-performance solar cell application, Adv. Mater. (2018) 30, 1800710.

(42) Qui, Y., Liang, J., Zhang, Z., Deng, Z., Xu, H., He, M., Wang, J., Yang, Y., Kong, L., Chen, C.-C., Tuning the interfacial dipole moment of spacer cations for charge extraction in efficient and ultrastable perovskite solar cells, J. Phys. Chem. C (2021) 125, 1256–1268.

(43) Cao, Q., Li, P., Chen, W., Zang, S., Han, L., Zhang, Y., Song, Y., Two-dimensional perovskites: Impacts of species, components, and properties of organic spacers on solar cells, Nano Today (2022) 43, 101394.

(44) Prajongtat, P., Hannongbua, S., A combined theoretical and experimental study of $CH_3NH_3PbI_3$ containing AVAI films prepared via an intramolecular exchange process, J. Phys. Chem. C (2018) 122, 19705–19711.

(45) Perdew, J. P., Burke, K., Ernzerhof, M., Generalized gradient approximation made simple, Phys. Rev. Lett. (1996) 77, 3865‒3868.

(46) Benedek, N. A., Snook, I. K., Latham, K., Yarovsky, I., Application of numerical basis sets to hydrogen bonded systems: A density functional theory study, J. Chem. Phys. (2005) 122, 144102.

(47) Zangwill, A., Soven, P., Density-functional approach to local-field effects in finite systems: Photoabsorption in the rare gasses, Phys. Rev. A (1980) 21, 1561.

(48) Herges, R., Geuenich, D., Delocalization of electrons in molecules, J. Phys. Chem. A (2001) 105, 3214–3220.

(49) Lin, D.Y., Guo, B.-C., Dai, Z.-Y., Lin, C.-F., Hsu, H.-P., PbI_2 single crystal growth and its optical property study, Crystals (2019) 9, 589.

(50) Le Corre, V. M., Duijnstee, E. A., El Tambouli, O., Ball, J. M., Snaith, H. J., Lim, J., Koster, L. J. A., Revealing charge carrier mobility and defect densities in metal halide perovskites via space-charge-limited current measurements, ACS Energy Lett. (2021) 6, 1087–1094.

(51) Ahmad, S., Fu. P., Yu, S., Yang, Q., Liu, X., Wang, X., Wang, X., Guo, X., Li, C., Dion-Jacobson phase 2D layered perovskites for solar cells with ultrahigh stability, Joule (2019) 3, 794–806.

(52) Zhao, W., Dong, Q., Zhang, J., Wang, S., Chen, M., Zhao, C., Hu, M., Jin, S., Padture, N. P., Shi, Y., Asymmetric alkyl diamine based Dion-Jacobson low-dimensional perovskite solar cells with efficiency exceeding 15%, J. Mater. Chem. A (2020) 8, 9919–9926.

(53) Xu, Z., Lu, D., Dong, X., Chen, M., Fu, Q., Liu, Y., Highly efficient and stable Dion-Jacobson perovskite solar cells enabled by extended π-conjugation of organic spacer, Adv. Mater. (2021) 33, 2105083.

(54) Li, K., Yue, S., Li, X., Ahmad, N., Cheng, Q., Wang, B., Zhang, X., Li, S., Li, Y., Huang, G., Kang, H., Yue, T., Zafar, S. U., Zhou, H., Zhu, L., Zhang, Y., High efficiency perovskite solar cells employing quasi-2D Ruddlesden-Popper/Dion-Jacobson heterojunctions, Adv. Funct. Mater. (2022) 32, 2200024.

(55) Liu, C., Yang, Y., Chen, H., Xu, J., Liu, A., Bati, A. S. R., Zhu, H., Grater, L., Hadke, S. S., Huang, C., Sangwan, V. K., Cai, T., Shin, D., Chen, L. X., Hersam, M. C., Mirkin, C. A., Chen. B., Kanatzidis, M. G., Sargent, E. H., Bimolecularly passivated interface enables efficient and stable inverted perovskite solar cells, Science (2023) 382, 810–815.